Retrieval of Precipitation Profiles from Airborne Radar and Passive Radiometer Measurements: Comparison with Dual-Frequency Radar Measurements

J. A. WEINMAN

Department of Meteorology, University of Wisconsin, Madison, Wisconsin

R. MENEGHINI

Goddard Space Flight Center, Greenbelt, Maryland

K. NAKAMURA

Communication Research Laboratory, Tokyo, Japan

(Manuscript received 5 June 1989, in final form 16 February 1990)

ABSTRACT

This study compares precipitation rate profiles derived from a single frequency radar and radiometer with such profiles derived from a dual-frequency radar.

Measurements obtained during the 1985–86 CRL/NASA rain measuring experiment from airborne X- and Ka-band radars and an X-band passive microwave radiometer were used to derive rainfall rate profiles over the Atlantic Ocean. The rainfall retrieval employs the classical Hitschfeld-Bordan radar equation constrained by a measurement of the path integrated extinction derived from passive radiometry.

The path-integrated extinction obtained from the radiometric measurements was compared with that obtained from coincident dual-frequency radar reflection measurements from the ocean surface. The mean rainfall rate derived from the path-integrated extinction retrieved from the measured microwave radiances agreed within 25% with the mean rainfall rate obtained from the reflected radar signals.

An analysis of the errors in the retrieval algorithm showed that errors in the path-integrated extinction significantly affect the retrieved rainfall profiles near the surface. A least squares linear extrapolation of the profile in the lowest kilometer was used to revise the boundary condition in the retrieval. The profiles were solved iteratively until the rainfall rate at the surface was within the range of scatter about the linear profile at higher altitudes.

An optimization analysis was applied to the derivation of rainfall rate profiles retrieved from a dual-frequency radar data. The results of the retrieval were compared to those obtained from the radar–radiometer retrievals.

The availability of only an X-band radiometer limited the retrieval of rainfall rate profiles to maritime cases. It appears that it will be possible to measure rainfall under most conditions when radiometers operating at several higher frequencies become available on future airborne radar experiments.

1. Introduction

Latent heat is a prominent component of the energy budget of the atmosphere. The vertical distribution of latent heating is especially significant because it affects atmospheric stability. For example, Lau and Peng (1987) showed that the distribution of latent heat in tropical and convective systems affected the propagation speed of Kelvin waves that are intimately related to 30–60 day oscillations in the tropical atmosphere. Trenberth et al. (1988) recently demonstrated that rainfall anomalies off the coast of Peru in early 1988 contributed to the North American drought later that year. A crucial consideration in their study was knowledge of the altitude at which the latent heat was released into the atmosphere. Determination of the distribution of latent heat released in the tropical atmosphere thus becomes an urgently needed climatological measurement.

Latent heat profiles can be derived from measurements of the vertical distribution of hydrometeors by employing a cloud model as was done by Tao et al. (1990). In order to meet the need for global data on latent heating in the tropical atmosphere, measurements of precipitation in the tropics will be sought from a spaceborne Tropical Rainfall Measuring Mission (TRMM) that is now under development. Considerations in the development of this satellite are described by Simpson et al. (1988). This satellite mission will employ a radar that operates at 14 GHz and a dual-

Corresponding author address: Dr. James A. Weinman, Department of Meteorology, University of Wisconsin—Madison, 1225 West Dayton Street, Madison, WI 53706.

polarized, multispectral passive radiometer that operates at 18, 22, 37 and 85.6 GHz.

The purpose of the following study is to determine rainfall profiles from a single-frequency radar operating in conjunction with a passive radiometer. The role of strong extinction in the radar return upon the retrieved profile is considered. The resulting profiles are compared with those derived from dual-frequency radar measurements.

Whereas radars and passive microwave radiometers have been used separately to measure distributions of hydrometeor phase and density, or the equivalent rainfall rate, the combination of measurements from radars and radiometers to retrieve rainfall rate distributions has only recently been implemented. Lu and Hai (1980) and Hai et al. (1985) employed an X-band radar and radiometer to measure rainfall rates from the ground. Airborne measurements of precipitation were also obtained from a dual frequency radar and a passive radiometer by Fujita et al. (1985); however the data from each instrument was analyzed independently in that study.

The employment of radars and radiometers in a downward pointing mode from satellite and aircraft platforms presents new problems as well as new opportunities to measure precipitation profiles. Because of size and weight limitations on antennae as well as resolution considerations, airborne radars operate at higher frequencies than those employed by operational ground-based weather radars. Attenuation thus becomes a serious limitation on the retrieval of rainfall rate profiles.

The present study will present the derivation of a modification of the Hitschfeld-Bordan (1954) algorithm to retrieve profiles of extinction coefficient under attenuating conditions. The path integrated extinction obtained from measurements of microwave radiances is invoked as a constraint on that radar retrieval algorithm. This is followed by an analysis that shows the nonlinear effect of errors in the path integrated extinction and noise in the measurements on the retrieved profiles of the extinction coefficient.

This analysis is applied to data obtained from a dual-frequency X- and Ka-band radar and an X-band radiometer. These data were obtained from airborne instrumentation on flights that occurred during a 1985–86 Communications Research Laboratory/NASA rain measuring experiment over the Atlantic Ocean near Wallops Island, Virginia. The radar and radiometric measurements are analyzed in the following manner:

1) Brightness temperatures computed from a radiative transfer model are compared to X-band brightness temperatures measured over the sea to infer the X-band path integrated extinction. The mean rainfall rate is derived from the mean extinction coefficient.

2) The mean rainfall rate derived from the X-band path integrated extinction is compared with that quantity derived from dual-frequency measurements of the radar power reflected from the sea surface in the presence of precipitation.

3) The Ka-band path integrated extinction of the rain below the radar in computed by inserting the mean rainfall obtained in step 1 into an appropriate expression that relates the extinction coefficient and the rainfall rate.

4) The two path integrated extinctions are used as constraints on the solutions to the radar equations at each corresponding frequency to provide profiles of the extinction coefficients. The extinction coefficients then yield rainfall rate profiles by using appropriate relationships between extinction coefficients and rainfall rates.

5) The precipitation profiles derived from strongly extinguished Ka-band data utilize a boundary value at the surface that is linearly extrapolated from the profile above .25 km.

6) The rainfall rate profile derived at those altitudes where only rain exists, is used to compute the instrument constant. This parameter is then used to derive the ice hydrometeor "rainfall rate" profile at those altitudes where the temperature is less than −35°C so that only ice hydrometeors may be expected to occur. The rainfall rate profile between the heights of the 0°C isotherm and the −35°C isotherm is obtained by interpolating between the rainfall rates obtained at those two altitudes.

7) The rainfall rate profiles retrieved from combined radar radiometric measurements are then compared to optimized profiles derived from the dual-frequency radar measurements. The Lagrange multiplier used in the optimization is a function of the error in the rainfall profile produced by uncertainties that may be expected in retrievals at each frequency.

2. Radar and radiometric instrumentation

The X- and Ka-band radars and radiometers were flown during the CRL/NASA experiment; however only data from the X-band radiometer and both radars are considered in this study. The instrumentation used in this study is characterized by the parameters cited in Table 1. This system has been described by Okamoto et al. (1982).

3. Theory of precipitation rate profile retrievals

a. Determination of the path-integrated extinction

1) Retrieval of the path-integrated extinction from X-band radiometry

The extinction coefficient, $k(z)$, in dB km^{-1} is a function of altitude, z, measured from the surface. Extinction by the liquid hydrometeors, by the ice hydrometeors and by the nonprecipitating cloud drops is represented by $k_l(z)$, $k_i(z)$ and $k_{cl}(z)$ respectively. Ka-

TABLE 1. Characteristics of the C.R.L. airborne sensors.

Radar:	X-Band	Ka-Band
Frequency (GHz)	10	34.45
Magnetron peak power (Kw)	20	10
Pulse repetition rate (Hz)	440	440
Pulse duration (μs)	0.5	0.5
Receiver bandwidth (MHz)	2	2
Receiver noise figure (dB)	5.3	9.6
Dynamic range (dB)	80	80
Number of samples	128	128
Antenna, offset paraboloid: (common to both radar and radiometer)		
Diameter (cm)	26	7.5
Scan angle (°) (All devices viewed nearly the same rain volume.)	±23 (operated at nadir in this study)	
Gain (dB)	26	26
3 dB beamwidth (°)	8.0 × 8.0	8.0 × 8.0
Radiometer:		
Type, null-balancing Dicke		
Noise figure (dB)	6	
Integration time (s)	.25	
Temperature resolution (K)	.5	
Absolute accuracy (K)	±2	
Dynamic range (K)	50–400	

band absorption by oxygen and water vapor is comparable to that expected from rainfall rates of 2 mm h^{-1}, which is negligible compared to the errors in the retrieved rainfall rates. Gaseous extinction is even less for X-band radiation. We assume that the former two of these extinction coefficients depend upon the rainfall rates, R, as

$$\tilde{k}\,(\text{dB km}^{-1}) = \alpha R^{\beta}\,(\text{mm h}^{-1}) \qquad (1)$$

where the constants α and β depend upon the frequency of the radiation and the phase of the hydrometeors. These constants are presented in Table 2. The values for liquid hydrometeors are taken from Atlas et al. (1984) and those for ice hydrometeors are fitted to the theoretical results of Kummerow and Weinman (1988) that were derived from an ensemble of hydrometeors whose sizes were characterized by an exponential size distribution.

The values of the extinction coefficient of the nonprecipitating liquid cloud drops are also presented in Table 2. The nonprecipitating liquid drops are assumed to be distributed with a constant density of 0.4 gm m^{-3} from the cloud base at 2 km to the cloud top, z^*, or to the flight altitude, H, whichever was the lowest.

The extinction coefficient of the precipitation is

$$\tilde{k}(z) = k(z) - k_{cl}(z)\,. \qquad (2)$$

A first-order estimate of the rain within the cloud was obtained from a radiative transfer model that relates the X-band emitted radiance to the path integrated extinction:

$$\tau\,(\text{dB}) = \int_0^{z^*} \tilde{k}(z')dz' = \bar{k}z^* \qquad (3)$$

where $\tilde{k}(z)$ is the X-band extinction coefficient of the rain and $\bar{k}$ its mean value. The X-band extinction coefficient is relatively insensitive to ice hydrometeors.

Height of various noteworthy levels are shown in Fig. 1. The height of the 0°C isotherm is z_0 and z_m is the height of the −35°C isotherm beyond which no liquid hydrometeors are expected. The maximum height to which only liquid precipitation may be expected is z^*.

The temperature profile is assumed to diminish linearly at a lapse rate of 6.5 K km^{-1} from the value at the surface, namely 20°C. The sea surface temperature is 15°C. These are representative air and sea surface temperatures around the U.S. East Coast in June. The value of z^* is thus 3.5 km.

A one-layer plane-parallel radiative transfer model was used to compute the X-band radiances in units of brightness temperature as a function of slant path integrated extinction, τ/μ, where μ is the cosine of the viewing angle. The model assumed that only liquid hydrometeors were present up to the level, z^*. Details of the derivation of that model were presented by Weinman and Davies (1978). The results that pertain to a plane-parallel cloud obtained in that study are cited in the Appendix of this paper. The input parameters used in that model are summarized in Table 2. The extinction coefficients, given in km^{-1}, employed in the radiative transfer model can be obtained by di-

TABLE 2. Parameters used to compute radiative quantities.

	Liquid		Ice	
Frequency (GHz)	10	35	10	35
α (dB/km)	.013	.219	.00024	.013
β	1.16	1.04	1.22	1.42
D (mm^6/m^3)	275	450	4100	10000
d	1.55	1.15	1.00	.84
A_1	−3.65	—	—	—
A_2	.453	—	—	—
A_3	−.028	—	—	—
G_0 (0°C)	.054	—	—	—
G_1 (0°C)	−.00020	—	—	—
G_2 (0°C)	−.016	—	—	—
k_{cl} (dB/m) (0°C)	.037	.416	—	—
$\lvert K\rvert^2$ (0°C)	.928	.882	.197	.197

* The radiative parameters for liquid water were computed at the ambient temperatures for each level; the values at 0°C are selected to be representative.

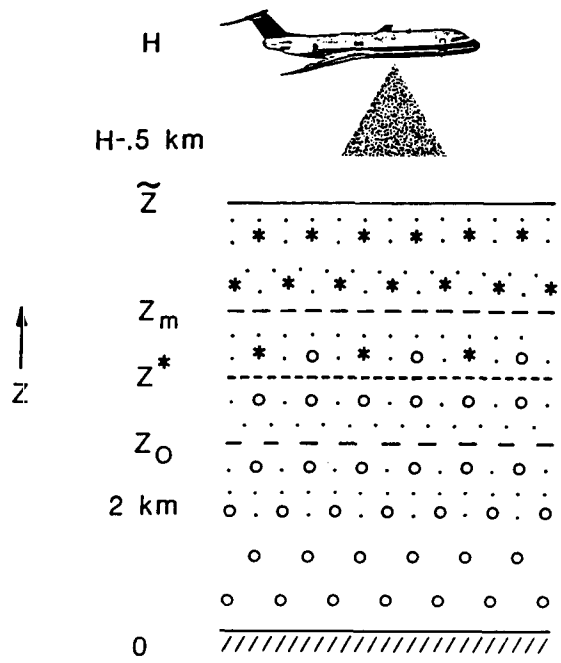

FIG. 1. Schematic view of the rainfall profile retrieval showing the various heights at which various hydrometeors occur in the present analysis. (.) nonprecipitating cloud drops, (*) ice hydrometeors, (O) rain. The following heights are: z_0, height of the 0°C isotherm; z^*, top of the rain layer (400 m above the freezing level); z_m, height of the −35°C isotherm; $\tilde{z}$, top of the precipitating cloud.

viding those cited in Table 2, given in dB km^{-1}, by 4.343.

The model radiances presented as brightness temperatures are a nonlinear function of the path integrated extinction. We are, however, interested in obtaining the inverse result, namely the path integrated extinction as a function of X-band brightness temperature, I, in K. A simple analytical expression that is accurate of 5% was fitted to the output of the model.

$$\tau/\mu\,(\text{dB}) = 7.12 - 1.42\ln[263.3 - I(\text{K})],$$
$$110\text{ K} < I < 257\text{ K},\quad 0.7 < \mu < 1. \quad (4)$$

The passive radiometric retrieval thus provides the mean rainfall rate, $\bar{R}$, from Eqs. (1), (3) and (4). More detailed information on rainfall profiles over land as well as the sea may ultimately be derived once several higher frequency microwave radiometric channels become available by utilizing the precipitation profile retrieval technique of Kummerow et al. (1989).

2) Derivation of the path-integrated extinction in the Ka-band

Once the mean rainfall rate, $\bar{R}$, within the rain column is determined from the X-band radiometric measurements, the path integrated extinction can be derived for Ka-band radar retrievals by employing Eqs. (1), (3) and (4) with the α and β appropriate to 35 GHz, see Table 2.

3) Derivation of the path-integrated extinction by dual-frequency radar methods only

Using radar data only, the path integrated extinction was determined by means of a Dual-wavelength Surface Reference Technique (DSRT) over the ocean, see Meneghini et al. (1987). These measurements provided a validation of the radiometrically derived τ.

For a down viewing airborne radar in the presence of rain along the beam, the backscattered power from the surface depends upon the path integrated extinction along the beam and the scattering cross section of the surface, σ_0. Because both τ and σ_0 are unknown, a measurement made at a neighboring rain free location, $\tilde{\sigma}_0$, can provide an estimate σ_0. If the surface returns exceed both the rain echo and the receiver noise at the range corresponding to $z = 0$, then the largest source of error arises from fluctuations in $\tilde{\sigma}_0/\sigma_0$. Nadir viewed data taken over a wind roughened ocean at wind speeds between 1 and 20 m/s produce a change that is less than 10 dB, see Jones et al. (1977).

In the dual-frequency version of this method, the differential path integrated attenuation estimate takes the form:

$$\Delta\tau = \int_0^{z^*} [k_{35}(z') - k_{10}(z')]dz$$
$$= \frac{1}{\gamma} \times \ln(\tilde{P}_{35}(0)P_{10}(0)/P_{35}(0)\tilde{P}_{10}(0)) \quad (5)$$

where $P_i(0)$ and $\tilde{P}_i(0)$ are the powers reflected from the sea surface at $z = 0$ beneath the rain column and from a nearby rain free region respectively at the frequencies designated by i and $\gamma = 0.461$.

The primary advantage of the DSRT compared to the single wave length version of the reflection technique is that the variance of the estimate of $\Delta\tau$ is reduced to the extent that σ_0 is correlated at the two frequencies.

b. *Retrieval of rainfall rate profiles from single-frequency radar and path-integrated extinction measurements*

1) Retrieval of rainfall extinction profiles from radar returned power

The nadir viewing radar measures the mean signal, $\bar{P}_s$, and noise power, $\bar{P}_n$, from N samples that are summed at the output of a square law detector. The backscattered signal power is

$$\bar{P}_s(z) = C' \frac{|K|^2 Z(z)}{(H-z)^2} \exp\left(-\gamma \int_z^{z^*} k(z')dz'\right), H > z^* \quad (6)$$

where the radar on the aircraft at height, H, measures

the power that has been scattered from the altitude, z. The liquid hydrometeor cloud extends to a height of z^*. If the aircraft flight altitude, H, is less than z^*, then z^* must be replaced by H. A minor problem must be overcome if $z^* > H$, namely the radar does not respond to precipitation within 500 m of the aircraft. The rain within that range interval extinguishes the backscattered signal but no scattered signal can be measured, see Fig. 1.

The constant, C', contains instrument parameters such as the emitted power, antenna area, efficiency of detection of the backscattered power and the pulse length that determines the volume from which the signal is measured.

The backscattering coefficient is proportional to $|K|^2 Z(z)$. This quantity varies with altitude and its value depends on the phase and the rainfall rate of the hydrometeors.

$$Z\,(\mathrm{mm}^6\ \mathrm{m}^{-3}) = DR^d\,(\mathrm{mm\ h}^{-1})\,. \tag{7}$$

For heights less than z^* all of the hydrometeors are assumed to be liquid and the hydrometeors are assumed to be dry graupel above z_m. The dependence of the backscattering coefficients on the rainfall rate are taken from the work of Douglas (1964). Table 2 also presents the values of the constants D and d that apply to X- and Ka-band radar scattering.

The term

$$|K| = \left|\frac{m^2 - 1}{m^2 + 2}\right| \tag{8}$$

where the complex refractive index, $m = n' - ik'$, depends upon the phase of the hydrometeors and the temperature. Representative values at 0°C are also shown in Table 2.

An estimate of $\bar{P}_s(z)$, designated $\hat{P}_s(z)$, can be obtained by subtracting an independent estimate of the noise power, $\hat{P}_n$, from the total measured power, $\hat{P}_t$:

$$\hat{P}_s(z) = \hat{P}_t(z) - \hat{P}_n. \tag{9}$$

Denoting the number of independent samples by N and the mean noise power by $\bar{P}_n$, then the mean and variance of $\hat{P}_t$ are $(\bar{P}_s + \bar{P}_n)$ and $(\bar{P}_s + \bar{P}_n)^2/N$, respectively, and the mean and variance of $\hat{P}_n$ are $\bar{P}_n$, $\bar{P}_n^2/N$. These relationships imply that $\hat{P}_s(z)$ is unbiased, $E\{\hat{P}_s(z)\} = \bar{P}_s(z)$, with a variance (see Ulaby et al. 1982)

$$\sigma^2(z) = \{[\bar{P}_s(z) + \bar{P}_n]^2 + [\bar{P}_n]^2\}/N\,. \tag{10}$$

The estimate, $\hat{P}_s(z)$, now can be written as

$$\hat{P}_s(z) = \bar{P}_s(z) + g(z) \tag{11}$$

where $g(z)$ is a random variable of zero mean whose variance is given by Eq. (10) and where $\bar{P}_s(z)$ is given by Eq. (6).

We can define a normalized estimate of the signal power, $S(z)$, by correcting the estimator of $\bar{P}_s$ for the extinction due to cloud liquid water and by removing the inverse square range dependence:

$$S(z) = \frac{(\bar{P}_s(z) + g(z))(H - z)^2}{(C'|K|^2)} \exp\left(\gamma \int_2^{z^*} k_{cl}(z')dz'\right) \tag{12}$$

where the limits of integration extend from the cloud base at 2 km to the cloud top, z^*. The random variable, $g(z)$, is neglected in the considerations remaining in section 3b(1); we will however return to a consideration of its effect in section 3b(2).

Recall that the backscattering and the extinction coefficients both depend on the rainfall rate to a power, so that

$$\tilde{k}(z) = cZ(z)^\eta. \tag{13}$$

Inserting Eq. (13) into Eq. (6), combining constants so that $C = C'/c$ enables the constant C' to be replaced by C and

$$S(z) = \tilde{k}(z)^{1/\eta} \exp\left(-\gamma \int_z^{z^*} \tilde{k}(z')dz'\right) \tag{14}$$

which is a function only of the extinction coefficient of the hydrometeors.

Taking logarithms of both sides of Eq. (14) and differentiating that equation with respect to z, yields:

$$\frac{d\ln S(z)}{dz} = \frac{1}{\eta\tilde{k}(z)} \frac{d\tilde{k}(z)}{dz} + \gamma\tilde{k}(z). \tag{15}$$

A solution to this differential equation was presented by Hitschfeld and Bordan (1954). They used the value of the extinction coefficient closest to the radar as a boundary condition. In the case of a nadir viewing radar, the extinction coefficient at the top of the precipitating column is $\tilde{k}(z^*)$ and the solution is

$$\tilde{k}(z) = S^\eta(z) \Big/ \left(\frac{S^\eta(z^*)}{\tilde{k}(z^*)} - \eta\gamma \int_z^{z^*} S^\eta(z')dz'\right). \tag{16a}$$

If the extinction coefficient at the base of the precipitating column, $\tilde{k}(0)$, is used as a boundary condition, the solution becomes

$$\tilde{k}(z) = S^\eta(z) \Big/ \left(\frac{S^\eta(0)}{\tilde{k}(0)} - \eta\gamma \int_0^{z} S^\eta(z')dz'\right). \tag{16b}$$

An alternative to Eq. (16a) can be found by employing the path-integrated extinction defined in Eq. (3) to derive the $\tilde{k}(z^*)$. Integrating Eq. (16a) from 0 to z^* yields

$$\tilde{k}(z^*) = \frac{1 - \exp(-\eta\gamma\tau)}{\int_0^{z^*} S^\eta(z')/S^\eta(z^*)dz'} \tag{17}$$

Expressing $\tilde{k}(z^*)$ in terms of τ permits Eq. (17) to be introduced into Eq. (16a) to yield

$$\tilde{k}(z) = \frac{S^{\eta}(z)[1 - \exp(-\eta\gamma\tau)]}{\eta\gamma\left[\int_0^z S^{\eta}(z')dz' + \exp(-\eta\gamma\tau)\int_z^{z^*} S^{\eta}(z')dz'\right]} \quad (18)$$

see Meneghini et al. (1983) and Weinman et al. (1988).

2) ERRORS IN THE EXTINCTION COEFFICIENT PRODUCED BY NOISE AND THE SAMPLE SIZE IN THE RADAR RANGE BINS

Noise and sampling errors give rise to the term $g(z)$, which is a zero-mean random variable with a variance given by Eq. (10). The following presentation considers the effect of this error.

$$\frac{(\bar{P}_s(z) + g(z))(H - z)^2}{C|K|^2} = \tilde{k}(z)\exp\left(-\gamma\int_z^{z^*}\tilde{k}(z')dz'\right). \quad (19a)$$

To investigate the effects of signal variability on the estimate of $\tilde{k}$, we approximate $(\bar{P}_s(z) + g(z))$ by $(\bar{P}_s(z) \pm \sigma(z))$ and replace $\tilde{k}(z)$ by $\tilde{k}(z) + \delta\tilde{k}(z)$. Equation (19a) becomes

$$\frac{(\bar{P}_s(z) \pm \sigma(z))(H - z)^2}{C|K|^2} = (\tilde{k}(z) + \delta\tilde{k}(z)) \times \exp\left(-\gamma\int_z^{z^*}(\tilde{k}(z') + \delta\tilde{k}(z'))dz'\right). \quad (19b)$$

Assuming that $\gamma\int_z^{z^*}\delta\tilde{k}(z')dz'$ is small so that this term can be neglected, then on using Eqs. (18) and (19b) and noting that the true value of $\tilde{k}$ satisfies Eq. (19a) with $g(z) \to 0$, then

$$\delta\tilde{k}(z) = \mp\frac{(H - z)^2[1 - \exp(-\gamma\tau)]\sigma(z)}{C\gamma|K|^2\left[\int_0^z S(z')dz' + \exp(-\gamma\tau)\int_z^{z^*} S(z')dz'\right]} \quad (20)$$

We can substitute the values at the boundaries into Eq. (20) to estimate the range of variability of $\delta\tilde{k}(z)$. If we assume that $\bar{P}_n \gg \bar{P}_s(0)$ then $\sigma(0) = \sqrt{2}\bar{P}_n/\sqrt{N}$. Typically at the top of the rain column, $\bar{P}_s(z^*) \gg \bar{P}_n$ so that $\sigma(z^*) = \bar{P}_s(z^*)/\sqrt{N}$. These approximations provide a relationship between errors in the extinction coefficient at the boundaries of the atmosphere:

$$\delta\tilde{k}(0) = \frac{\sqrt{2}\bar{P}_n H^2\exp(\gamma\tau)}{\bar{P}_s(z^*)(H - z^*)^2}\delta\tilde{k}(z^*). \quad (21)$$

The extinction coefficient error produced by noise power and the finite radar integration sampling is a function of the signal-to-noise ratio at the top of the precipitating column, and it increases near the ground because of corrections for the range-squared and path-integrated extinction.

3) ERRORS IN THE EXTINCTION COEFFICIENT PRODUCED BY ERRORS IN THE PATH-INTEGRATED EXTINCTION

Errors in the path-integrated extinction, $\delta\tau$, produce errors in the retrieved extinction coefficient profile, $\delta\tilde{k}(z)$. For simplicity in the subsequent discussion we will assume that the extinction coefficient, $\tilde{k}(z)$, can be represented by the mean value, $\bar{k}$, from Eq. (3) and that $\eta = 1$.

Considering the effect of an error in the path integrated extinction on Eq. (17) yields

$$\tilde{k}(z^*)(1 + \delta\tilde{k}(z^*)/\tilde{k}(z^*)) = \frac{1 - \exp[-\gamma\tau(1 + \delta\tau/\tau)]}{\gamma\int_0^{z^*} S(z')/S(z^*)dz'} \quad (22)$$

Subtracting Eq. (17) from Eq. (22) and dividing that difference by Eq. (17) yields

$$1 + \delta\tilde{k}(z)/\bar{k} = \left\langle\left\{(1 - \exp[-\gamma\tau(1 + \delta\tau/\tau)]\right\} \times \exp\left(\gamma\int_z^{z^*}\delta k(z')dz'\right)\right\rangle \times [1 - \exp(-\gamma\tau)]^{-1} \quad (23)$$

A quantity, $\xi(z) = 1 + \delta\tilde{k}(z)/\bar{k}$, can then be inserted into Eq. (23) and the result can be differentiated to yield

$$\frac{d\xi}{dz} = -\gamma\bar{k}\xi(\xi - 1). \quad (24)$$

This differential equation can be readily integrated and $\delta\tilde{k}(z)$ can be found

$$\frac{\delta\tilde{k}(z)}{\bar{k} + \delta\tilde{k}(z)} = \frac{\delta\tilde{k}(z^*)}{\bar{k} + \delta\tilde{k}(z^*)}\exp[\gamma\bar{k}(z^* - z)]. \quad (25)$$

Tedious, but straightforward algebraic manipulation yields

$$\delta\tilde{k}(z) = \{\bar{k}\exp(-\gamma\bar{k}z)[1 - \exp(-\gamma\delta\tau)]\} \times \langle\{1 - \exp[-\gamma(\tau + \delta\tau)]\} - \exp(-\gamma\bar{k}z)[1 - \exp(-\gamma\delta\tau)]\rangle^{-1}. \quad (26)$$

In the case of light rainfall rates where $\tau \to 0$, the error in the retrieved extinction coefficient at the surface, $\delta\tilde{k}(0)$, is proportional to the mean extinction and the fractional error in the path integrated extinction, i.e.

$$\delta\tilde{k}(0) = \bar{k}\delta\tau/\tau. \quad (27)$$

It is especially instructive to see how the $\delta\tilde{k}(0)$ varies

as the path-integrated extinction becomes large, $\tau \to \infty$. In that case

$$\delta\tilde{k}(0) = \bar{k}[\exp(\gamma\delta\tau) - 1]. \quad (28)$$

The error in the retrieved extinction coefficient thus increases exponentially with the error in the path integrated extinction if that error is positive. The error in the retrieved extinction coefficient approaches $-\bar{k}$ if the error in the path integrated extinction is negative, so that the retrieved extinction coefficient approaches 0.

The results given by Eqs. (21) and (28) show that at ranges near the surface, the effects of sampling, small signal: noise ratios, and errors in the path-attenuation estimate may in some cases lead to large overestimates in the derived rain rate (attenuation) profile.

4) Derivation of rainfall rate profiles from returned radar power with erroneous path-integrated extinction

In order to reduce the effect of errors in the path-integrated extinction on the retrieved extinction coefficient profile, we seek profiles of the extinction coefficient that eliminate the large excursions near the surface derived in Eq. (26). This is achieved by applying a least squares linear fit to the profile of the extinction coefficient, $\tilde{k}_i(z)$, between the altitudes 0.25 and 1 km to produce a new profile, $\tilde{k}_{i+1}(z)$. Extrapolation to the surface yields a revised estimate of $\tilde{k}_{i+1}(0)$. If $d\tilde{k}_{i+1}(0)/dz > 0$ and $\tilde{k}_{i+1}(0) > \tilde{k}_i(0)$, or if $d\tilde{k}_{i+1}(0)/dz < 0$ and $\tilde{k}_{i+1}(0) < \tilde{k}_i(0)$, then the new value of $\tilde{k}_{i+1}(0)$ can be inserted into Eq. (16b) and the profile can be re-derived. This procedure is repeated until the profile falls within the limits defined by the scatter in the retrieval about the fitted least squares linear profile between 0.25 and 1 km. If these conditions are not satisfied, then the original profile, $\tilde{k}_i(z)$, is kept.

The profile of the rainfall rate is obtained from the extinction coefficient profile by applying Eq. (1).

5) Retrieval of the ice hydrometeor profile above the melting layer

Only ice hydrometeors are assumed to exist above the −35°C isotherm at z_m so that Eq. (7) can be used to determine the backscattering from ice hydrometeors.

The constant, C', that appears in Eq. (6) was determined for both the X- and Ka-band returns by matching the returned power computed from the rainfall rate profile to the measured signal power, $\bar{P}_s(z)$, at levels where the signal/noise ratio is large and the phase of the hydrometeors is known, i.e., such that there is little likelihood of encountering melting hail.

The extinction due to ice hydrometeors can be neglected in the topmost cloud layer and the backscatter coefficient can be used to derive the "rainfall rate" of that layer. The extinction that affects the return from the next layer can be derived from the preceding layer and the backscatter coefficient can be used to compute the "rainfall rate" of the ice hydrometeors in each layer down to z_m.

6) Retrieval of the rainfall rate in the melting layer

The extinction and backscattering coefficients in the melting layer are complicated functions of the rainfall rate because the phase of the hydrometeors is changing with height. Accordingly, the "rainfall rate" for $z_0 < z < z_m$ is represented by a parabolic curve that is fitted in a least square sense to layers below z_0 and above z_m.

c. Retrieval of rainfall profiles from dual-frequency radar measurements only

In order to determine the validity of the retrieval described in section 3b, optimized rain rate profiles were obtained from the combined dual frequency radar returns. We define a quantity that simultaneously minimizes the effects of errors and uncertainties in the retrievals obtained from radar measurements at both frequencies:

$$\psi = \text{minimum} = \int_0^{z^*} [R_0(z') - R_{35}(z')]^2 + \Lambda(z')[R_0(z') - R_{10}(z')]^2 dz'. \quad (29)$$

The Lagrange multiplier in this case is proportional to the ratio of the two quadratic terms that appear in Eq. (29), i.e.

$$\Lambda(z') = \frac{\left[\dfrac{\{[\tilde{k}(z') + \delta\tilde{k}(z')]^{1/\beta} - \tilde{k}(z')^{1/\beta}\}R(z')}{\tilde{k}(z')^{1/\beta}}\right]_{35}^2}{[f(z')R(z')]^2} \quad (30)$$

where the denominator is proportional to the error introduced by the scatter about the least squares linear fit to the lower part of the Ka-band retrieval of the extinction coefficient profile. The numerator is proportional to the uncertainty in the rainfall rate retrieved from the X-band radar; it is caused by hail or mixed phase precipitation that is most likely above 1 km. The uncertainty in the rainfall retrieved from the X-band radar is proportional to a fractional part, $f(z')$, of the retrieved rainfall profile, $R(z')$.

Setting the derivative of ψ with respect to $R_0(z')$ to zero yields

$$R_0(z) = \frac{R_{35}(z) + \Lambda(z)R_{10}(z)}{[1 + \Lambda(z)]}. \quad (31)$$

Finally, the steps outlined in sections 3b (5 and 6) are repeated for the dual-frequency radar retrieval.

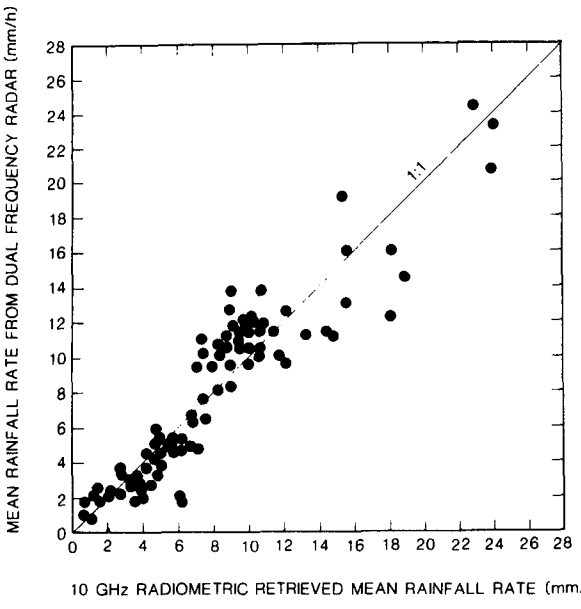

FIG. 2. Comparison of mean rainfall rates, $\bar{R}$, retrieved from the X-band passive microwave radiometer data and from the X- and Ka-band dual frequency radar reflections from the sea surface. Each point represents values of $\bar{R}$ inferred from coincident measurements.

4. Experimental results and discussion

a. Determination of path-integrated extinction from dual-frequency radar and from passive radiometric measurements and the effect of errors in that retrieval

The path integrated extinction was derived from the X-band measured radiometric brightness temperature. The path-integrated extinction was also determined by measuring the reflection of the radar power from the sea surface with both the X- and Ka-band radars. A comparison of the mean rainfall rates derived from Eqs. (1), (3) and (4) and from Eqs. (1), (3) and (5) is presented in Fig. 2. The two techniques provide average rainfall rates that agree within about 25%.

The effect of a fractional error in the path integrated extinction, $\delta\tau/\tau \approx 25\%$, that is given in Eq. (26), is demonstrated in Fig. 3. The curves that are shown were computed for the path integrated extinction values that were used to retrieve rainfall rate profiles from Ka-band returns. Those sample returns are identified by the numbers shown in the parentheses. Note that the error increases abruptly at the surface if $\delta\tau > 0$ whereas diminishes more smoothly for $\delta\tau < 0$. For the cases that were analyzed. $2.55 < z^* < 3.5$ km, the errors are most significant below 0.25 km. The least squares linear fit described in section 3b(4) was therefore derived from data above 0.25 km.

The mean rainfall rates, $\bar{R}$, for the samples that were used in this study are presented in the captions of Figs. 4b, 5b, 6b and 7b. These mean rainfall rates were inferred from the path integrated extinction derived from the radiometric brightness temperature. The mean rainfall rates derived from the path integrated extinction obtained from the DSRT are also cited.

b. Retrieval of profiles of rainfall rates from single frequency radar and passive radiometric measurements and from dual-frequency radar returns

Examples of returned range square corrected radar power and noise profiles are presented in Figs. 4a, 5a, 6a and 7a. Because the noise in the X-band was negligible, only the Ka-band noise is presented. We applied the algorithm to Ka-band radar returns even though we had to derive the path integrated extinction for that channel from the mean rainfall rate obtained from the X-band radiometric value. This was done because we wish to illustrate the impact of strong extinction and serious noise effects upon the retrieved profiles. It is evident from these figures that noise becomes significant for returned Ka-band radar power scattered near the surface under heavy rainfall conditions.

Figures 4b to 7b show four examples of rainfall rate profiles retrieved by means of the algorithms described in section 3.

Figure 4b compares the precipitation retrieval profiles obtained from X- and Ka-band radars with constraints imposed by the path integrated extinction. The present algorithm appears to operate in the presence

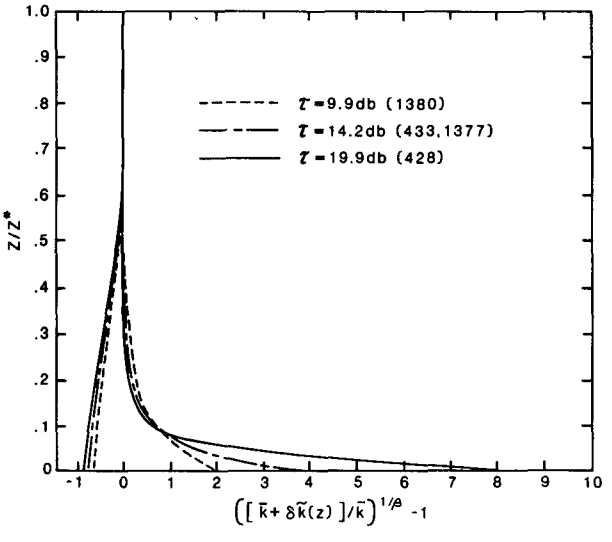

FIG. 3. Profile of the fractional errors in the rainfall rates retrieved from a uniform rain column whose Ka-band path-integrated extinction is in error by $\pm\delta\tau/\tau = 25\%$. The curves that are shown were computed from Eq. (26) for the values that correspond to the samples whose profiles are displayed in the subsequent figures. The sample numbers are identified in the parentheses. These errors are plotted against the normalized altitude, z/z^*.

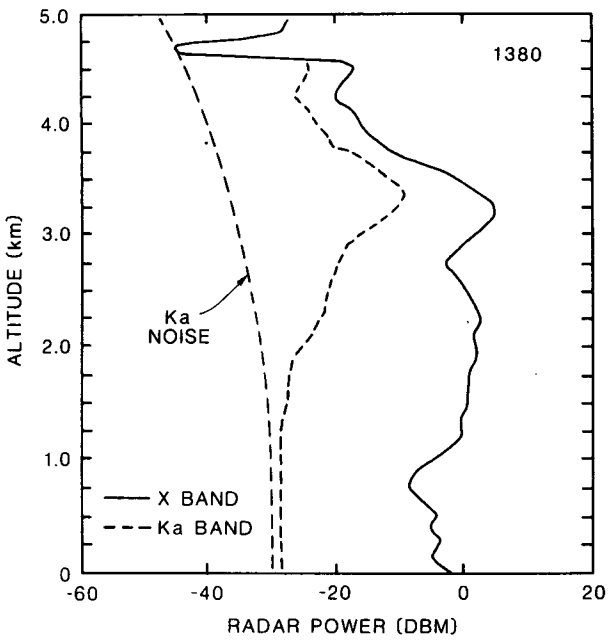

FIG. 4a. Profiles of the range square corrected returned radar power in dB for X- and Ka-band radars for sample 1380. The Ka-band range square corrected noise in dB is also shown.

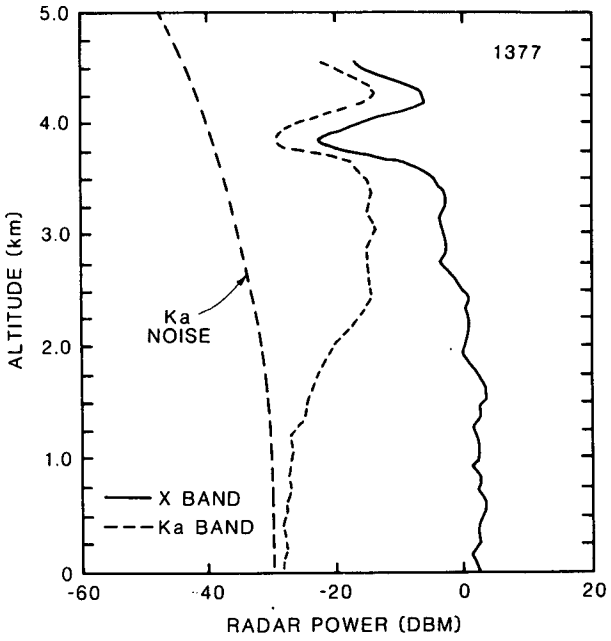

FIG. 5a. As in Fig. 4a but for sample 1377.

of ice and melting hydrometeors provided that all of the ice hydrometeors remain above the 0°C level. It is noteworthy that the Ka-band retrieval below 1.25 km approaches 9 mm h^{-1}, where the algorithm tends to replace the dubious part of the retrieval with the extrapolated value of the rainfall rate. Because the rainfall retrieved from the Ka-band radar does not diminish as that derived from the X-band radar retrieval below 1 km, it cannot increase as much above 2 km and still preserve the path integrated extinction. The dual-frequency radar retrieved profile follows the Ka-band return near the top of the rain layer and it follows the X-band return near the surface where an erroneous

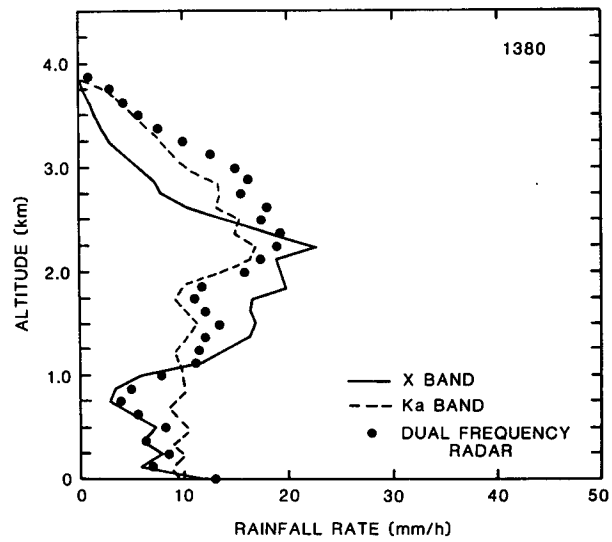

FIG. 4b. Profiles of rainfall rate (mm h^{-1}) retrieved from the algorithm that combines single frequency radiometric and radar data. These results are compared to those obtained from the dual frequency radar algorithm, (•). The data is derived from sample 1380 for which H = 5.1 km, I = 176.6 K, $\bar{R}$ (radiometric) = 11.9 mm h^{-1} and $\bar{R}$ (Dual-wavelength Surface Reference Technique) = 12.8 mm h^{-1}.

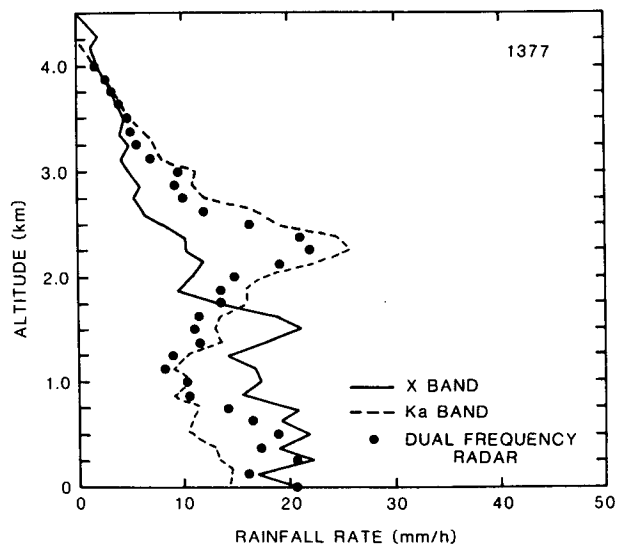

FIG. 5b. As in Fig. 4b but for sample 1377; H = 5.1 km, I = 186.7 K, $\bar{R}$ (radiometric) = 14.0 mm h^{-1} and $\bar{R}$ (DSRT) = 13.0 mm h^{-1}.

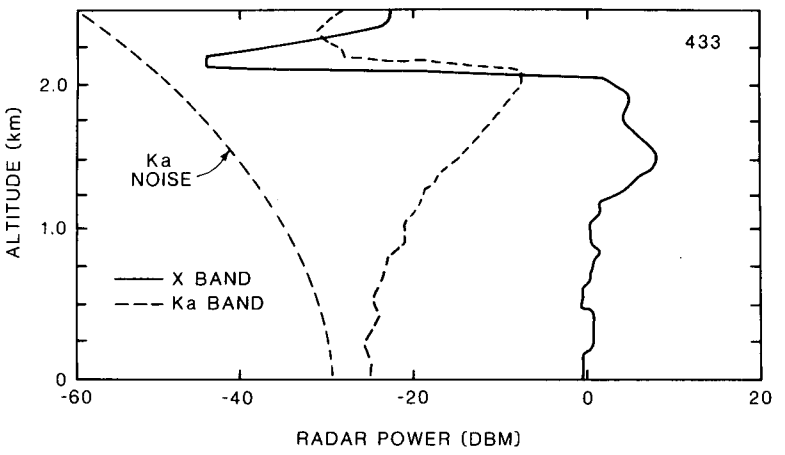

FIG. 6a. As in Fig. 4a but for sample 433.

Ka path-integrated extinction renders that data unacceptable.

Figure 5b is an example of inconsistently retrieved rainfall rate profiles. Inspection of Fig. 5a reveals that the retrieved profiles are compatible with the data but that data appears to behave inconsistently. The peak at 2.25 km is consistent with the sample that is shown in Fig. 4 while the monotonic increase in the X-band retrieval is consistent with the sample that is shown in Fig. 7. This difficulty may have been caused by the sensors that were sampling different volumes, or the drop size distribution may not have been correctly described as a Marshall–Palmer distribution. This case illustrates some problems that require additional attention.

The optimized dual-frequency radar retrieval follows the profile retrieved from the X-band measurements near the surface and switches to the profile retrieved from the Ka-band data above 2 km.

Figure 6b compares the rainfall rate profiles retrieved from data in the probable presence of melting graupel at an altitude of 1.5 km. The X-band radar return is more sensitive to such graupel than is the Ka-band radar. The agreement between the two profiles is excellent at all altitudes other than this region; the Ka-band tends to retrieve higher rainfall rates at altitudes other than 1.5 km to maintain the expected path integrated extinction. This example points out a limitation of operating with only an X-band radar if only a single radiometer channel is available. Had a multifrequency passive radiometer ensemble been available, then the altitude and density of ice hydrometeors could have been estimated and the retrieval algorithm could have been corrected, see Kummerow et al. (1990).

The rainfall profile retrieved from the dual-frequency radar again follows that retrieved from the Ka-band radar at high altitudes and approaches the profile obtained from both of the radar–radiometer combinations.

Figure 7b shows X- and Ka-band retrievals that are in excellent agreement. The reason for that appears to be that the signal/noise ratio was acceptable for both radar returns and no ice hydrometeors appear to have been present in this case. It is noteworthy that both the X- and Ka-band retrievals continue their monotonic trends near the surface. The dual-frequency radar rainfall retrieval again falls between the two radar–radiometer retrievals.

5. Conclusions

Brightness temperatures measured with an X-band passive microwave radiometer were used to infer the

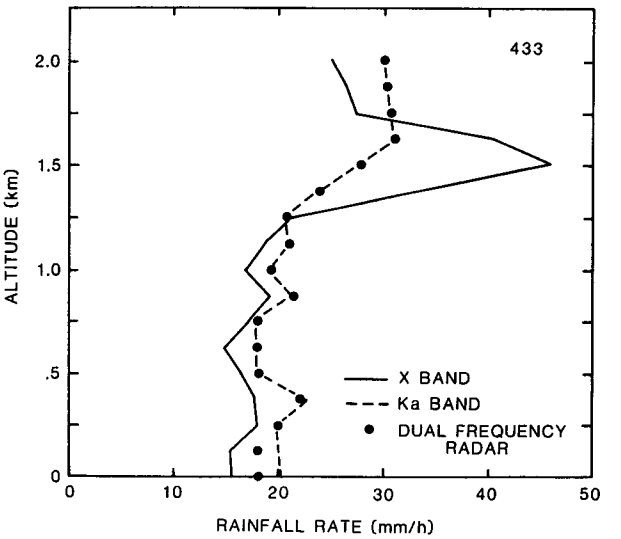

FIG. 6b. As in Fig. 4b but for sample 433; H = 2.55 km, I = 202.0 K, $\bar{R}$ (radiometric) = 22.8 mm h^{-1} and $\bar{R}$ (DSRT) = 20.7 mm h^{-1}.

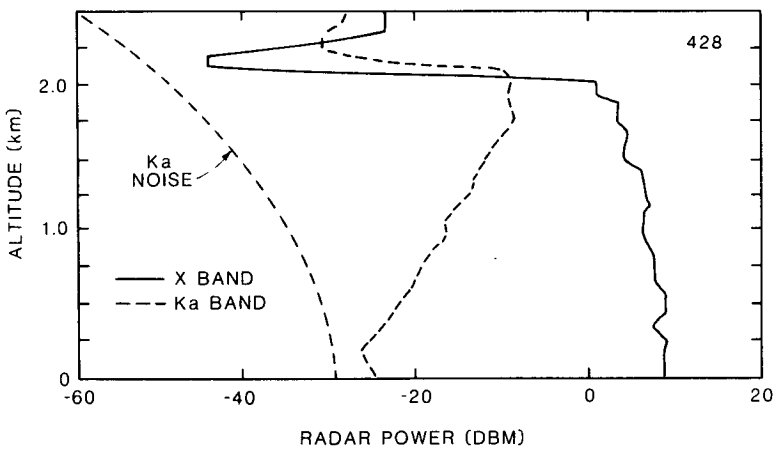

FIG. 7a. As in Fig. 4a but for sample 428.

path-integrated extinction produced by raincloud. This quantity was then used to determine the mean rainfall rate in the clouds that contained rain. The results of this technique were compared with those obtained from measurements of the path-integrated extinction that were obtained from the reflection from the sea surface with a dual-frequency radar. It was shown that the mean rainfall rates determined by these two techniques were consistent to within 25%.

The path-integrated extinction provided a constraint on the radar equation that permitted rainfall rate profiles to be determined in the presence of strong extinction. An analysis of the errors inherent in such a retrieval suggested that derived rainfall rate was most sensitive to erroneous path-integrated extinction near the surface under heavy precipitation. A solution to the radar equation, based on the expected departure of the rainfall rate profile near the surface, was developed to yield retrievals from noisy and erroneous data. The results of this analysis were compared to rainfall rate profiles derived from dual-frequency radar data. If no melting graupel existed below the freezing level, the retrieved profiles suggest that combining data from a single frequency radar and a radiometer can provide rainfall rate profiles that are consistent with profiles derived from a dual-frequency radar to within about 30%.

Figures 5 and 6 suggest that care will be needed to assure that radars and radiometers view the same volumes.

The present technique is applicable only over the ocean if a single-frequency radiometer is used. Space and airborne rain observation systems now utilize or are planned to utilize multifrequency radiometers. Approximate estimates of the path integrated extinction and the hydrometeor phase profile can be derived from such data, see Kummerow et al. (1989). Multifrequency radiometers may remove some of the ambiguities produced by varying phase or size distributions.

In view of these findings, a single-frequency radar operating in conjunction with multifrequency passive radiometers shows promise of being able to provide cost effective space-borne measurements of tropical rainfall distributions. However, a dual-frequency radar would be very beneficial to remove some ambiguities that were encountered in this study.

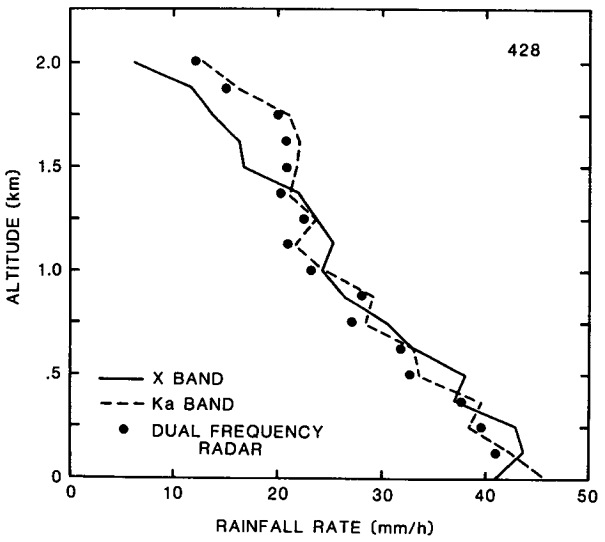

FIG. 7b. As in Fig. 4b but for sample 428; H = 2.55 km, I = 212.0 K, $\bar{R}$ (radiometric) = 26.5 mm h^{-1} and $\bar{R}$ (DSRT) = 28.9 mm h^{-1}.

Acknowledgments. We wish to thank Drs. Joanne Simpson and Chris Kummerow of the Goddard Space Flight Center and Art Jameson of A.R.C. for numerous helpful discussions on radiometry, radar and severe storm meteorology.

APPENDIX

One-Layer Radiative Transfer Model

A one-layer plane-parallel radiative transfer model based upon the second Eddington approximation was developed to derive radiances, $I(z^*, \theta)$, emerging from z^* at a viewing angle, θ. The radiances are presented in units of equivalent brightness temperature, K. This model considers absorption and scattering.

Only the mean values of the extinction coefficient, $\bar{k}$, the albedo for single scattering, a, and the asymmetry factor, g, are used in this model. The extinction coefficients in Table 2 must be divided by 4.343 to convert them to units of km^{-1} so that they can be used in the following formalism. The surface emissivity, ϵ, and the surface temperature, T^*, define the lower boundary condition and B_0 defines the temperature at the cloud top height, z^*. A uniform lapse rate B_1 characterizes the temperature profile in the model.

Details of the derivation of this model were presented by Weinman and Davies (1978). An analytical representation of the radiance emerging from the top of a column of rain is:

$$I(z^*, \theta) = \sum_{i=1}^{4} I_i + \exp(\bar{k}z^*/\mu)\left\{\epsilon T^* + [1-\epsilon] \times \left[D_+\left(1-\frac{\lambda}{h}\right)\exp(\lambda z^*) + D_-\left(1+\frac{\lambda}{h}\right) \times \exp(-\lambda z^*) + B_1\left(z^* - \frac{1}{h}\right) + B_0\right]\right\} \quad \text{(A1)}$$

$$I_i = (\Gamma_i/\gamma_i)\{[\exp(\gamma_i z^*)] - 1\} \quad i = 1, 2, 3 \quad \text{(A2a)}$$

$$I_4 = (\Gamma_4/\gamma_4^2)\{1 - [\exp(\gamma_4 z^*)](1 - \gamma_4 z^*)\} \quad \text{(A2b)}$$

$$\Gamma_1 = -\frac{\bar{k}aD_+}{\mu}\left(1 - \frac{3g\lambda\mu}{2h}\right) \quad \gamma_1 = \frac{\bar{k}}{\mu} + \lambda \quad \text{(A2c)}$$

$$\Gamma_2 = -\frac{\bar{k}aD_-}{\mu}\left(1 + \frac{3g\lambda\mu}{2h}\right) \quad \gamma_2 = \frac{\bar{k}}{\mu} - \lambda \quad \text{(A2d)}$$

$$\Gamma_3 = -\frac{\bar{k}}{\mu}\left(B_0 - \frac{3ga\mu B_1}{2h}\right) \quad \gamma_3 = \gamma_4 = \frac{\bar{k}}{\mu} \quad \text{(A2e)}$$

$$\Gamma_4 = -\frac{\bar{k}}{\mu}B_1 \quad \text{(A2f)}$$

$$D_+ = \left\{\left(\frac{B_1}{h} - B_0\right)\left[\epsilon - \frac{(2-\epsilon)\lambda}{h}\right]\exp(-\lambda z^*) + \left[\frac{B_1(2-\epsilon)}{h} + \epsilon(B_0 + B_1 z^* - T^*)\right] \times \left(1 + \frac{\lambda}{h}\right)\right\}\Big/\Delta \quad \text{(A3a)}$$

$$D_- = -\left\{\left(\frac{B_1}{h} - B_0\right)\left[\epsilon + \frac{(2-\epsilon)\lambda}{h}\right]\exp(\lambda z^*) + \left[\frac{B_1(2-\epsilon)}{h} + \epsilon(B_0 + B_1 z^* - T^*)\right] \times \left(1 - \frac{\lambda}{h}\right)\right\}\Big/\Delta \quad \text{(A3b)}$$

and

$$\Delta = \left(1 - \frac{\lambda}{h}\right)\left[\epsilon - \frac{(2-\epsilon)\lambda}{h}\right]\exp(-\lambda z^*) - \left(1 + \frac{\lambda}{h}\right)\left[\epsilon + \frac{(2-\epsilon)\lambda}{h}\right]\exp(\lambda z^*). \quad \text{(A3c)}$$

The dependence of the extinction coefficient upon the mean rainfall rate, $\bar{R}$, is given by Eq. (1). The asymmetry factor is represented by

$$g = G_0 + G_1\bar{R} + G_2\ln(\bar{R}) \quad \text{(A4a)}$$

and the albedo for single scattering is

$$a = \exp(A_1 + A_2\ln(\bar{R}) + A_3[\ln(\bar{R})]^2) \quad \text{(A4b)}$$

These parameters appear in

$$h = 3\bar{k}(1 - ag)/2 \quad \text{(A4c)}$$

$$\lambda = \bar{k}\sqrt{3(1-a)(1-ag)} \quad \text{(A4d)}$$

and

$$\mu = \cos(\theta). \quad \text{(A4e)}$$

The parameters used in the model are summarized in Table 2.

REFERENCES

Atlas, D., C. W. Ulbrich and R. Meneghini, 1984: The multiparameter remote measurement of rainfall. *Radio Sci.*, **19,** 3–22.

Douglas, R. H., 1964: Hail size distribution. *Proc. 11th Radar Weather Conf.*, Amer. Meteor. Soc., Boston, 146–149.

Fujita, M., K. Okamoto, S. Yoshikado and K. Nakamura, 1985: Inference of rain rate profile and path-integrated rain rate by an airborne microwave rain scatterometer. *Radio Sci.*, **20,** 631–642.

Hai, L., M. Xin and C. Wei, 1985: Ground based remote sensing of LWC in cloud and rainfall by a combined dual wavelength radar–radiometer system. *Adv. Atmos. Sci.*, **2,** 93–103.

Hitschfeld, W., and J. Bordan, 1954: Errors inherent in the radar measurement of rainfall at attenuating wavelengths. *J. Meteor.*, **11,** 58–67.

Jones, W. L., L. C. Schroeder and J. L. Mitchell, 1977: Aircraft measurements of the microwave scattering signature of the ocean, *IEEE.* **AP-25,** 52–61.

Kummerow, C. D., and J. A. Weinman, 1988: Radiative properties of deformed hydrometeors for commonly used passive microwave frequencies. *IEEE Trans. Geosci. Remote Sens.*, **26,** 629–638.

——, I. M. Hakkarinen, H. F. Pierce and J. A. Weinman, 1990: Determination of precipitation profiles from airborne passive microwave radiometric measurements. *J. Atmos. Oceanic Tech.*, submitted.

Lau, K. M., and L. Peng, 1987: Origin of low-frequency (intraseasonal) oscillations in the tropical atmosphere. Part I: Basic theory. *J. Atmos. Sci.,* **44,** 950–972.

Lu, D-r, and L. Hai, 1980: Comparisons of radar and microwave radiometer in precipitation measurements and their combined use. *Acta Atmos. Sinica,* **1,** 30–39.

Meneghini, R. J., J. Eckerman and D. Atlas, 1983: Determination of rain rate from a spaceborne radar technique. *IEEE Trans. Geosci. Remote Sens.,* **GE-21,** 34–43.

——, A. Jones and L. H. Gesell, 1987: Analysis of a dual-wavelength surface reference radar technique. *IEEE Trans. Geosci. Remote Sens.,* **GE-25,** 456–471.

Okamoto, K., S. Yoshikado, H. Masuko, T. Ojima, N. Fugono, K. Nakamura, J. Awaka and H. Inomata, 1982: Airborne microwave rain scatterometer/radiometer. *Int. J. Remote Sens.,* **3,** 277–294.

Simpson, J., R. F. Adler and G. R. North, 1988: A proposed Tropical Rainfall Measuring Mission (TRMM) satellite. *Bull. Amer. Meteor. Soc.,* **69,** 278–295.

Tao, W-K., J. Simpson, S. Lang, M. McCumber, R. Adler and R. Penc, 1990: An algorithm to estimate the heating budget from hydrometeor distributions. *J. Appl. Meteor.,* accepted.

Trenberth, K. E., G. W. Branstator and P. A. Arkin, 1988: Origins of the 1988 North American drought. *Science,* **242,** 1640–1645.

Ulaby, F. T., R. K. Moore and A. K. Fung, 1982: *Microwave Remote Sensing, Active and Passive.* Addison-Wesley, 476–495.

Weinman, J. A., and R. Davies, 1978: Thermal microwave radiances from horizontally finite clouds of hydrometeors. *J. Geophys. Res.,* **83,** 3099–3107.

——, C. D. Kummerow and C. S. Atwater, 1988: An algorithm to derive precipitation profiles from a downward viewing radar and a multifrequency passive radiometer. *Proc. of IGARSS '88 Symp.,* Edinburgh, Scotland, Ref. ESA SP-284. [IEEE 88CH2497-6.]